Lasers in Manufacturing Conference 2019

Effects of Beam Power and Power Density Distribution on Process and Quality Issues during Fiber Laser Cutting of Stainless Steel Sheet Metal

Dirk Petring[a*], Dennis Arntz[a], Stoyan Stoyanov[a], Frank Schneider[a]

[a]*Fraunhofer Institute for Laser Tehnology ILT, Steinbachstrasse 15, 52074 Aachen, Germany*

Abstract

Sheet metal fabricating industry implemented fiber laser cutting promptly due to being a more cost-efficient alternative to CO_2 laser beam cutting regarding investment as well as operation. Continuous technology improvements regarding available power levels as well as versatility in beam shaping provide further options for improved performance. However, with a lack of understanding of the underlying fundamentals, parameter optimization mainly takes place by trial and error. The multi-dimensional parameter space often impedes to find the real optimum and the associated rules. Process diagnostics and quality analyses combined with the simulation tool CALCut yield a deeper insight into the effects of beam properties on process and quality issues. Thereby, processing rules and their range of validity can be identified. Using the example of stainless steel cutting with beam powers between 5 and 10 kW and different power density distributions reveals how the cutting front and cut result can be deliberately affected.

Keywords: Laser beam cutting; fiber laser; process diagnostics; process simulation; process optimization; cut quality.

1. Introduction

The knowledge of parameter dependencies is a key expertise of process developers and engineers. This applies equally to the laser beam cutting process. Accordingly, with the advent and triumphal procession of multi-kW fiber and disk laser cutting machines since mid of the last decade a multitude of new parameter

* Corresponding author. Tel.: +49 241-8906210
E-mail address: dirk.petring@ilt.fraunhofer.de .

investigations has been carried out especially in the important market sector of fusion cutting of stainless steel sheet metal. If knowing appropriate parameters comes along with the understanding of the underlying fundamentals and rules, know-how advances to know-why. The latter not only permits the explanation but even the prediction of optimum parameter directions.

In laser beam cutting, industry has identified two major measures in order to gain better process performance: higher beam power and adapted beam power density distribution. System suppliers argue according to their special capabilities which of these measures is most beneficial. So far, there is no common understanding about the fundamental effects on cut flank quality.

This paper shall treat some so far widely neglected mechanisms of the laser beam cutting process and their effect on cut flank roughness and bottom edge burr formation. Process and quality diagnostics (Arntz et al., 2019) and process simulations with the software CALCut (Petring, 2016) shall enable a deeper insight into the fundamentals of laser beam fusion cutting of stainless steel. The used process parameters are readable from the figures and figure captions if not mentioned in the text. All experiments have been carried out with a TruDisk 12002 disk laser from TRUMPF.

First of all, in section 2. the changes of cutting front geometry, its surface temperature distribution and process variables such as average values of melt film surface temperature and thickness as well as bottom exit speed are calculated versus proportionally increasing beam power and cutting speed using the example of 15 mm thick stainless steel. In this thick sheet and low speed regime particularly effects on and of surface tension and melt viscosity are addressed.

In section 3. changes of cut flank roughness and of related streak images from high-speed videos of the cutting front vertex are determined experimentally for increasing cutting speed at constant beam power. Simulations of the corresponding cutting fronts and properties of the melt and vapor flow indicate characteristic variations of physical process variables providing plausible explanations.

Finally, in section 4. trends of burr formation at varied sheet thickness, beam power and cutting speed are tested experimentally and correlated with the calculated contribution of lateral mass flow.

In the conclusion statements are summarized about how cut quality is susceptible to laser beam power, power density distribution and related cutting speeds.

2. Changes of process variables with proportionally increasing beam power and cutting speed

The changes of cutting front geometry, its surface temperature distribution and process variables such as average values of melt film surface temperature and thickness as well as bottom exit speed are calculated versus proportionally increasing beam power and cutting speed, i.e. at a constant energy per unit length being 0.4 kJ/mm, using the example of 15 mm thick stainless steel.

According to the simulations in fig. 1 the calculated cutting front geometries indicate a more regular and laterally extended shape for higher powers and speeds. This becomes most obvious by looking at the contours of cutting front vertex and flank. Also an effect of the power density distribution can be read from fig. 1. A positive influence on the regularity and an even more pronounced lateral extension of the cutting front is identified for a ring-shaped instead of a Gaussian-like power density distribution at high powers and speeds.

A rise of the cutting speed requires and results in elevated melt film temperatures (see fig. 2). Especially in the thick sheet and generally rather low speed regime investigated here, temperature dependencies of surface tension and melt viscosity have to be addressed (see fig. 3).

The sulfur content in standard stainless steels (up to 150 ppm) reduces the surface tension compared to pure iron in the lower temperature range near the melting point and leads to a change of sign of the surface tension gradient along corresponding temperature gradients. Accordingly, the maximum surface tension

indicated by a yellow line in fig. 3 does not occur at the phase boundary but at elevated temperatures and at diminished values of the surface tension. For a sulfur content of 80 ppm a maximum at 2180 K is estimated by extrapolation from measured values of Li et al., 2005. The corresponding isotherm is indicated in the cutting front simulations in fig. 1 by a yellow line, too.

Along these isotherms, the melt film particularly tends to accumulate to strings as the regime of maximum surface tension attracts melt. With increasing speed, due to elevated surface temperatures and increasing temperature gradients this curved string is shifted more and more in the direction of the phase boundaries of the melt film surface, i.e. the melting boundary at the top leading edge and at the resolidification line on the cutting flank. The melt film gets tightened from the boundaries and thereby stabilized, and yet at an overall low level of surface tension – allowing wetting.

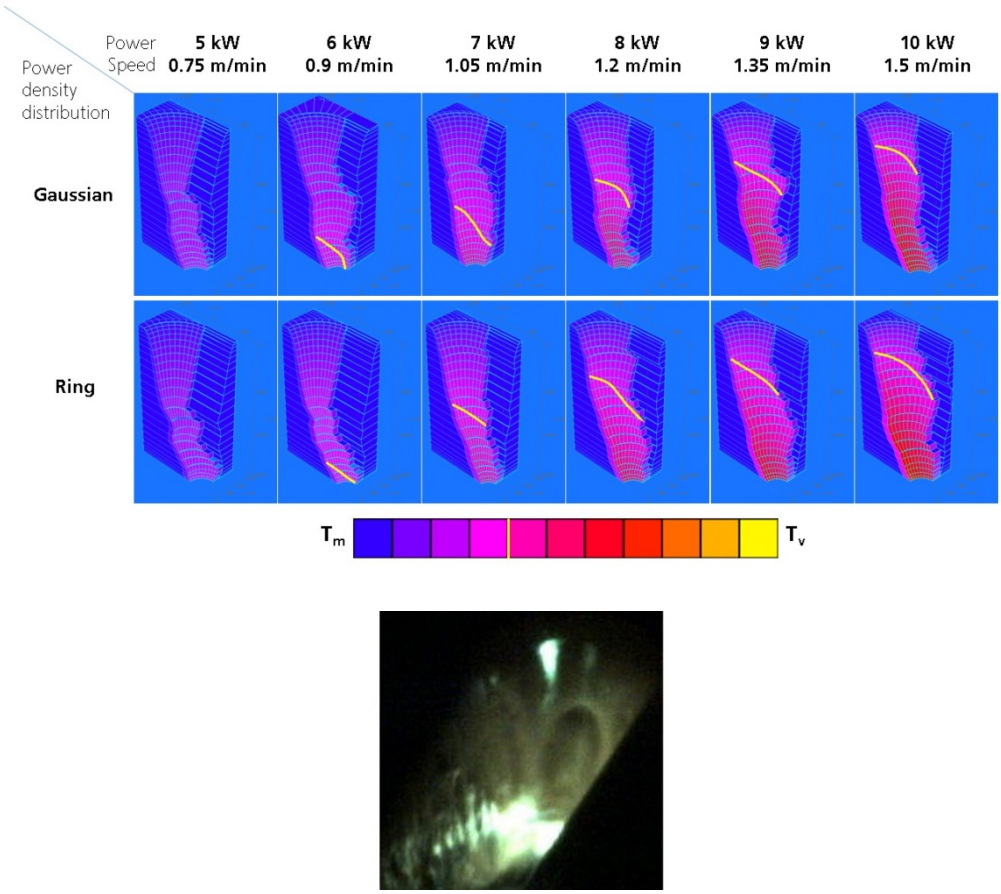

Fig. 1. Calculated cutting fronts and surface temperature distributions for varied laser powers and cutting speeds at constant energy per unit length for Gaussian-like and ring-shaped power density distributions. The yellow lines indicate the curved 2180 K isotherms. Other parameters: 15 mm stainless steel, beam quality 8 mm*mrad, focal diameter 630 µm, focal position +9 mm, Nitrogen 2 MPa. The bottom picture shows an exemplary high-speed video frame demonstrating a curved melt string (view from top right onto the cutting front).

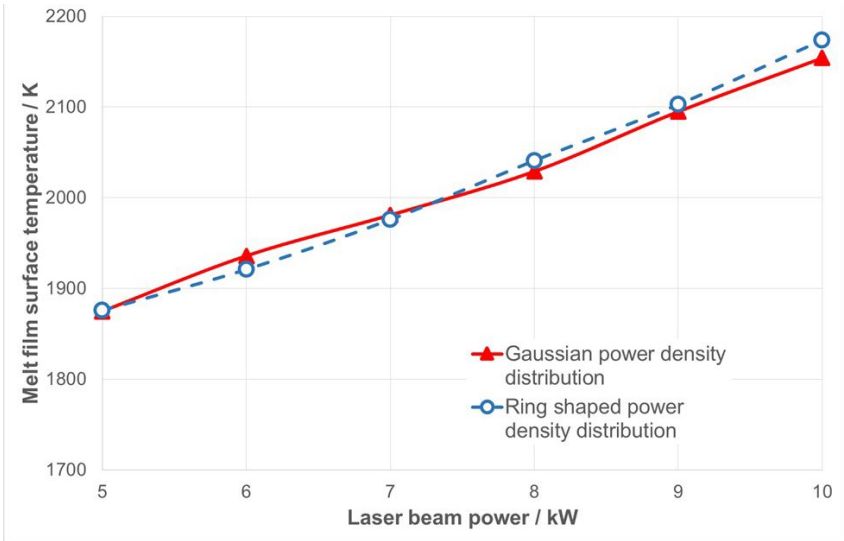

Fig. 2. Average melt film surface temperature versus laser beam power at constant energy per unit length. Other parameters see fig. 1.

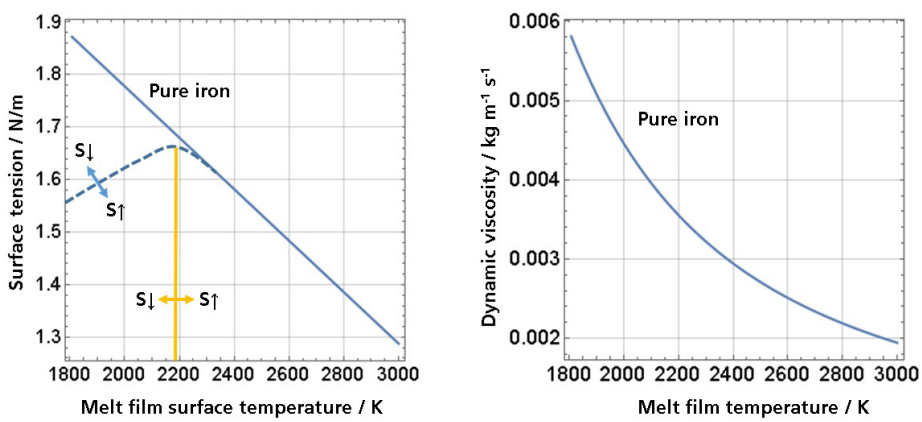

Fig. 3. Left: Surface tension versus melt film surface temperature for pure iron (solid line) and standard stainless steel with sulfur content S=80 ppm (dashed line). Arrows up and down indicate changes due to increasing or decreasing sulfur content S, respectively. The values for stainless steel are extrapolated from measurements by Li et al., 2005. Right: Dynamic viscosity of molten iron versus melt film temperature. All values for iron are taken from Brandes, 1983.

According to fig. 3 with increasing sulfur content string formation on the front is shifted to higher temperature regimes, i.e. to deeper cut depths, and diminishes. On the other hand, the maximum surface tension at the phase boundary declines and facilitates smooth wetting of the cut flank. This explains the beneficial effect of higher sulfur content on the cutting performance of Cr/Ni-steels also at lower speeds recently described by Goppold et al., 2018.

In addition, elevated melt film temperatures reduce the melt viscosity (see fig. 3). This enhances the fluidity of the melt, fostering melt acceleration by all contributing driving forces, namely gas flow, surface tension gradients and – if appearing – vapor pressure gradients, the latter being discussed in the next sections.

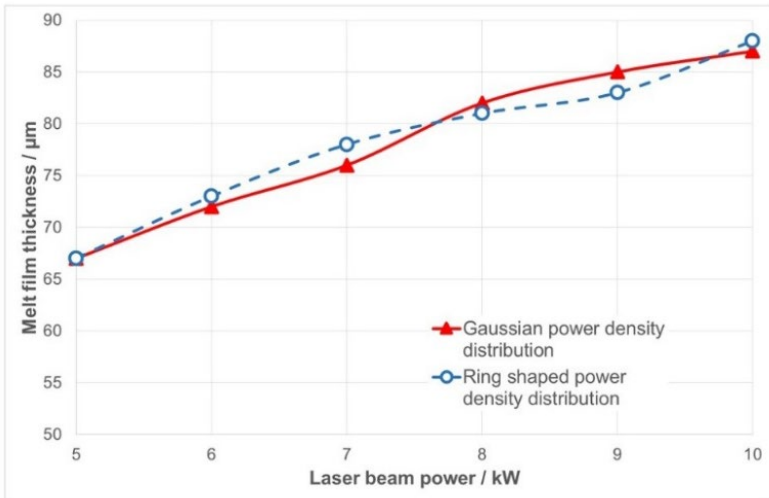

Fig. 4. Average melt film thickness versus laser beam power at constant energy per unit length. Other parameters see fig. 1.

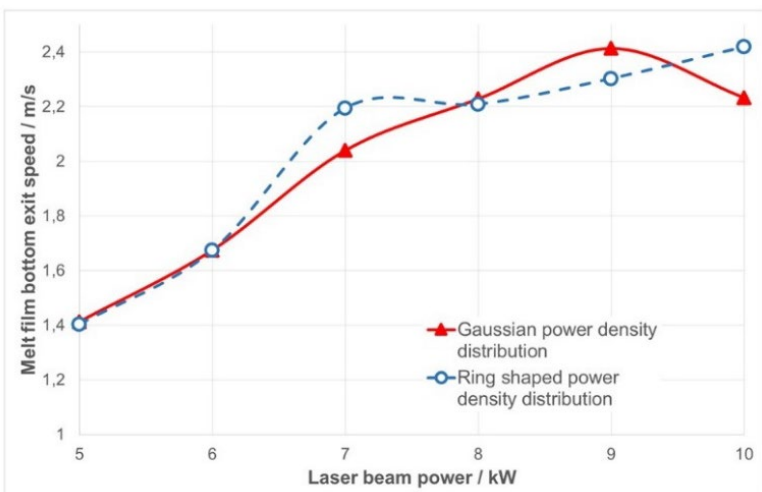

Fig. 5. Melt film bottom exit speed versus laser beam power at constant energy per unit length. Other parameters see fig. 1.

Fig. 4 illustrates the calculated increase of average melt film thickness due to increased material removal rate to be mastered with increasing cutting speed. However, the increase in melt film thickness is underproportional e.g. because of the above explained, rising fluidity of the melt with temperature.

It is quite evident that according to the simulations also the bottom exit speed of the melt film increases with cutting speed. Remarkably, this increase saturates at a level around 2.3 m/s in the treated parameter regime (see fig. 5). The bottom exit speed varies around this value without a clear trend. Other transport mechanisms begin to contribute as discussed more detailed in the next sections.

3. Changes of cut flank roughness with increasing cutting speed at constant beam power

In this section, changes of cut flank roughness and of related streak images produced from high-speed videos of the cutting front vertex are determined experimentally at increasing cutting speeds and constant beam power of 5 kW. The material is 6 mm stainless steel. Other parameters are listed in fig. 6.

Simulations of the corresponding cutting fronts and properties of the melt and vapor flow indicate characteristic variations of process variables providing plausible trends.

Two dominant effects are illustrated with the computer simulations in fig. 6. One is the significant change of the cutting front geometries regarding shape and inclination. The other is the significant change in temperature level and distribution.

Evaporation starts to be visible in the case of 2.8 m/min at a cutting depth of more than 5 mm (yellow colored parts of the cutting front surface), getting much more pronounced in the case of 3.8 m/min, where evaporation starts already at a cutting depth of about 3 mm on the cutting front vertex. From there downward, the evaporation regime gradually spreads towards the cutting flank.

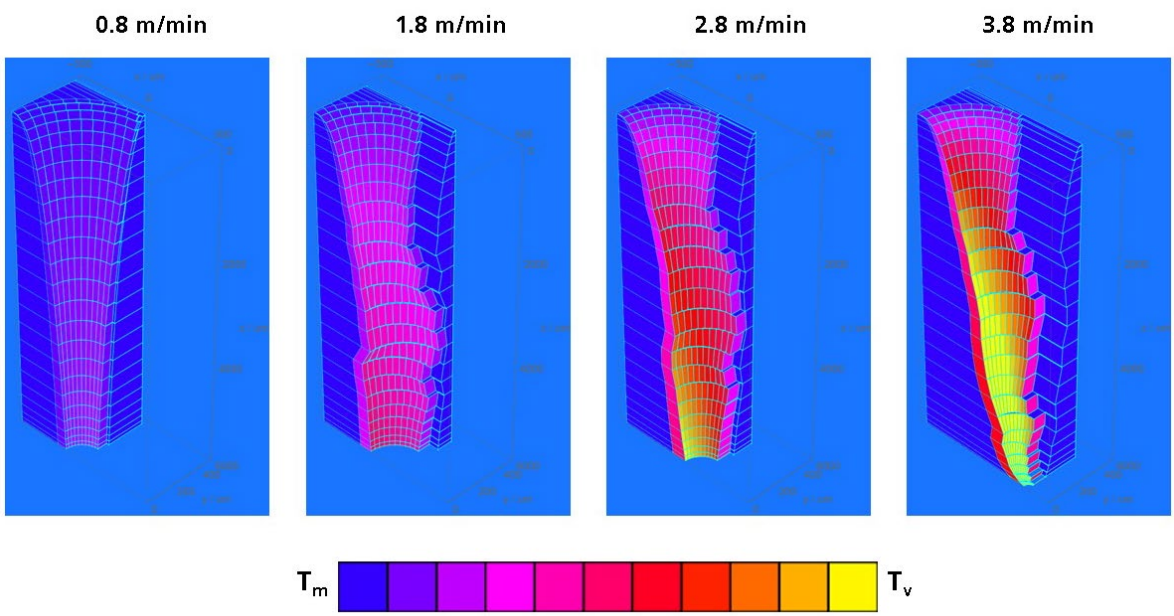

Fig. 6. Calculated cutting front geometries and surface temperature distributions for varied cutting speeds at constant laser beam power of 5 kW. (6 mm stainless steel, beam quality 8 mm*mrad, focal diameter 500 µm, focal position -4 mm, Nitrogen 2 MPa).

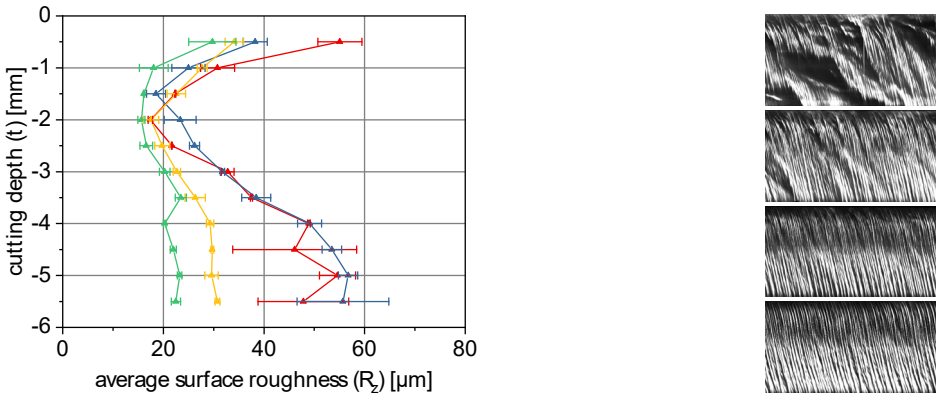

Fig. 7. Average surface roughness versus cutting depth (left) and related streak images of cutting front vertex (right) for varied cutting speeds (Arntz et al., 2019): 0.8m/min (red curve, streak 1st from top), 1.8m/min (blue curve, streak 2nd from top), 2.8m/min (yellow curve, streak 3rd from top), 3.8m/min (green curve, bottom streak). Other cutting parameters as defined in fig. 6.

Reduction of surface roughness with cutting speed correlates well with more regular streak images of high-speed videos of the cutting front vertex (see fig. 7).

Approaching or even exceeding the evaporation point leads to significant lateral melt acceleration due to the vapor pressure gradient along the temperature gradient developing predominantly in lateral direction (see the two most right simulations in fig. 6). This is a rather forceful effect as indicated by the strongly changing mass transport values depicted in fig. 8 d)-f). An increase of average melt film temperature and thickness, bottom exit speed as well as a progressive contribution of evaporation and lateral mass flow is calculated for the cuts with reduced roughness.

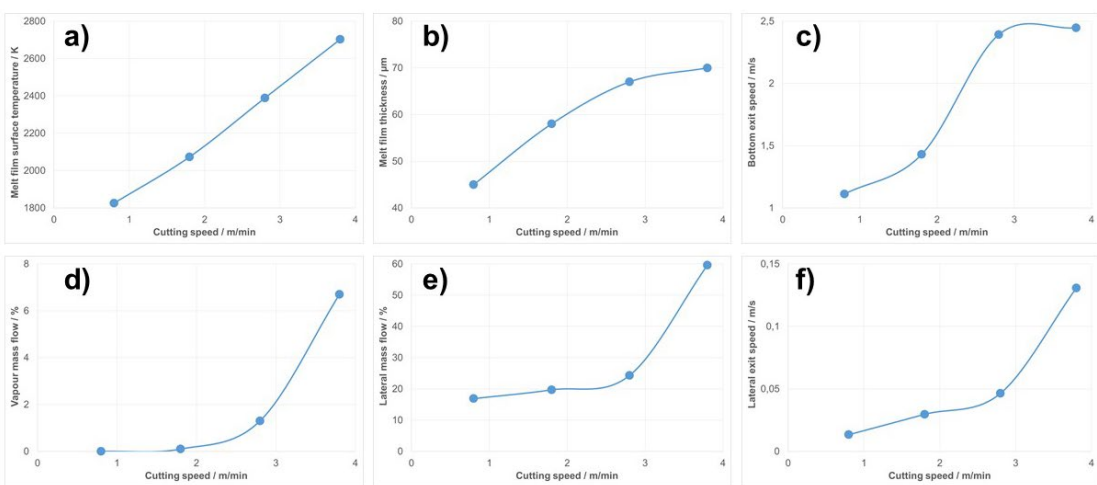

Fig. 8. Change of process variables (averaged over the cutting front where applicable) versus cutting speed. Cutting parameters as defined in fig. 6.

4. Trends of burr formation at varied sheet thickness, beam power and cutting speed

Trends of burr formation at varied sheet thickness, beam power and cutting speed are tested experimentally and compared with calculated melt film properties (see table 1). The stepwise 1-dimensional parameter changes across the 3-dimensional parameter space (sheet thickness, beam power, cutting speed) reveal that burr formation shows a stringent correlation with the lateral mass flow (see fig. 9). Only with increasing proportion of lateral mass flow from one parameter point to the next burr formation seems definitely to be reduced. Therefore, the consecutive parameter points of table 1 can all be linked by line sections with negative inclination in fig. 9. In contrast, melt film surface temperature and bottom exit speed do not reveal such a clear trend (see table 1).

Table 1. Parameter variation along a path in the three-dimensional parameter space of sheet thickness, beam power and cutting speed starting from line 5 with bold typed working point for a minimum of 0.11 mm of the maximum occurring burr length at this parameter. Fixed parameters: stainless steel, beam quality 8 mm*mrad, focal diameter 630 µm, focal position 0 mm, Nitrogen 2 MPa (Stoyanov et al., 2019).

Sheet thickness / mm	Beam power / kW	Cutting speed / m/min	Max. burr length / mm	Melt surface temperature / K	Bottom exit speed / m/s	Lateral mass flow / %
6	10	5.4	0.93	2954	1.68	79.6
6	10	4.5	1.09	2866	1.98	74.2
6	10	3.6	1.35	2699	2.14	43.2
6	8	3.6	0.75	2688	2.48	54.7
6	**6**	**3.6**	**0.11**	**2699**	**1.67**	**65.1**
6	6	1.8	0.56	2081	1.43	18.8
6	6	0.9	2.45	1850	1.11	15.2
15	6	0.9	1.31	1910	2.40	25.8
15	8	0.9	1.42	1922	1.52	19.6
15	10	0.9	1.80	1927	1.46	17.2
15	10	1.35	1.46	2086	2.41	23.3

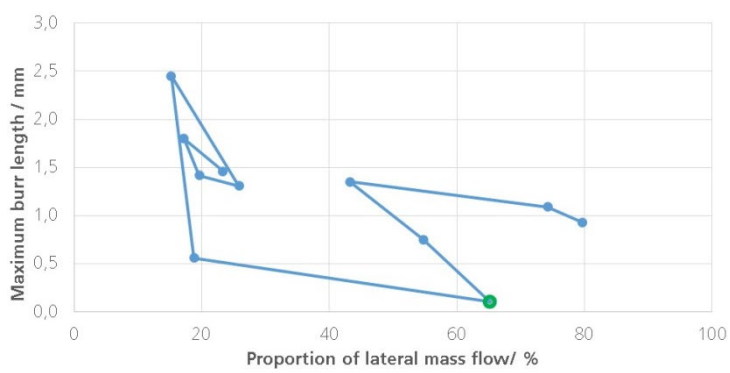

Fig. 9. Stringent trend with positive correlation between increasing proportion of lateral mass flow and decreasing burr length in either case.

5. Conclusion

The following statements about how cut quality is susceptible to laser beam power, power density distribution and related cutting speeds are derived for fusion cutting of stainless steel with 1 micron wavelength:

- Increasing beam power enables improved cut quality by allowing higher cutting speed. Corresponding simulations of the cutting front geometry tend to show a more regular shape.
- Higher cutting speed requires and results in elevated melt film temperatures.
- Elevated melt film temperatures shift the surface tension over its maximum to the regime declining with temperature and reduce the melt viscosity. The first effect produces melt accumulations forming curved strings being shifted to the solid boundaries of the cutting front at further elevated temperature levels. The second effect increases the fluidity of the melt fostering melt acceleration by all contributing driving forces (gas flow, surface tension gradients and – if appearing – vapor pressure gradients).
- Approaching or even exceeding the evaporation point leads to significant lateral melt acceleration due to the vapor pressure gradient along the temperature gradient developing predominantly in lateral direction.
- Reduction of surface roughness with increasing cutting speed correlates well with more regular streak images of high-speed videos of the cutting front vertex.
- An increase of melt film temperature, thickness and downward speed as well as a progressive contribution of evaporation and lateral mass flow is calculated for the cuts with reduced roughness.
- Burr formation at varied sheet thickness, beam power and cutting speed shows a stringent correlation with the lateral mass flow. With its increasing proportion burr formation seems definitely to be reduced.
- Effects of the power density distribution have only been studied theoretically. A positive influence on the regularity and the lateral extension of the cutting front by using a ring-shaped instead of a Gaussian-like power density distribution could exemplarily be calculated for 15 mm stainless steel at high powers and speeds.

The above statements appear to be plausible but are partly still hypothetical in view of the limited range of tested parameters and the application of merely a steady-state simulation, namely CALCut. Moreover, the derived “rules” presume an adequate selection of the cutting gas parameters such as pressure, nozzle diameter and nozzle distance as well as of the beam focusing conditions such as focus diameter, beam quality and focal position. Without this, the described effects would be hidden by improper beam and gas jet propagation and excessively induced irregularities within the kerf. The complex interaction of all relevant process parameters and their effect on the distribution of the dominant process variables at the cutting front and flank remains the most challenging aspect of further work to be performed.

Acknowledgements

The experimental parts of this work were carried out complementarily within the framework of the Collaborative Research Centre SFB1120-236616214 “Precision Melt Engineering” and within the Cluster of Excellence “Internet of Production” at the Chair of Laser Technology LLT of RWTH Aachen University and the Fraunhofer Institute for Laser Technology ILT and funded by the Deutsche Forschungsgemeinschaft e.V. (DFG, German Research Foundation). The sponsorship and support is gratefully acknowledged.

References

Arntz, D., Petring, D., Schneider, F., Poprawe, R., 2019. In situ high speed diagnosis—A quantitative analysis of melt flow dynamics inside cutting kerfs during laser fusion cutting with 1 µm wavelength. Journal of Laser Applications, Vol. 31, 022206.

Arntz, D., Petring, D., Schneider, F., Stoyanov, S., Halm, U., Gillner, A., 2019. "Quantitative analysis of the temporal distance between melt waves on the cutting front apex during laser fusion cutting of stainless-steel sheet metal with 1 micron wavelength," Proc. of Lasers in Manfacturing Conference, Munich, Germany (these proceedings).

Brandes, E. A., 1983. *Smithells Metals Reference Book,* 6th edition, Butterworths, London, UK.

Goppold, C., Urlau, F., Pinder, T., Herwig, P, Lasagni, A. F., 2018. Experimental investigation of cutting performance for different material compositions of Cr/Ni-steel with 1 µm laser radiation. Journal of Laser Applications, Vol. 30, 031501.

Petring, D., 2016. "Virtual Laser Cutting Simulation for Real Parameter Optimization", Proceedings of JLPS 84th Laser Materials Processing Conference, Nagoya, Japan, pp. 11-20.

Li, Z., Mukai, K., Zese, M., Mills, K.C., 2005. Determination of the surface tension of liquid stainless steel. JOURNAL OF MATERIALS SCIENCE 40, pp. 2191–2195.

Stoyanov, S., Arntz, D., Petring, D., 2019. "Investigation on the melt ejection and burr formation during laser fusion cutting of stainless steel," Proc. of 38th ICALEO, Orlando, USA (to be published).